

Using Fixed-Potential Electrodes To Quantify Iron And Manganese Redox Cycling In Upland Soils

Caitlin Hodges (✉ chodges@ou.edu)

The University of Oklahoma <https://orcid.org/0000-0003-3960-5771>

John M. Regan

The Pennsylvania State University

Brandon Forsythe

The Pennsylvania State University

David Oakley

The Pennsylvania State University

Jason Kaye

The Pennsylvania State University

Susan L. Brantley

The Pennsylvania State University

Research Article

Keywords:

Posted Date: March 11th, 2022

DOI: <https://doi.org/10.21203/rs.3.rs-1319160/v1>

License:  This work is licensed under a Creative Commons Attribution 4.0 International License.

[Read Full License](#)

1 Using fixed-potential electrodes to quantify iron and
2 manganese redox cycling in upland soils

3 *Caitlin Hedges^{1*}, John M. Regan², Brandon Forsythe³, David Oakley⁴, Jason Kaye⁵, Susan L.
4 Brantley^{3,4}*

5

6 ¹University of Oklahoma, School of Geoscience, Norman, Oklahoma

7 ²Pennsylvania State University, Department of Civil and Environmental Engineering, University
8 Park, PA

9 ³Pennsylvania State University, Earth and Environmental Systems Institute, University Park, PA

10 ⁴Pennsylvania State University, Department of Geosciences, University Park, PA

11 ⁵Pennsylvania State University, Department of Ecosystem Science and Management, University
12 Park, PA

13

14 *Corresponding Author: Caitlin Hedges, chodges@ou.edu

15

16 KEYWORDS: Anaerobic respiration, soil respiration, critical zone, mineral weathering,
17 anaerobic microsites

18 ABSTRACT

19 Changes in metal redox in soils can exert strong controls on carbon mineralization but are
20 difficult to measure in real time. Recently, potentiostatically poised electrodes (fixed-potential
21 electrodes) have been demonstrated as promising for measuring the rate of oxidation and reduction
22 at a specific reduction potential *in situ* in riparian soils but are yet untested in upland soils. Here
23 for the first time, we explored the fine-scale temporal fluctuations of redox of both iron and
24 manganese in response to environmental conditions. We used three-electrode systems with
25 working electrodes fixed at 100 mV (vs. SHE) in 2019 and added 400 mV in 2020 at 50 cm and
26 70 cm in the valley floor soil of a headwater watershed at the Susquehanna Shale Hills Critical
27 Zone Observatory (SSHCZO). Electrodes fixed at 100 mV mimic iron oxides and at 400 mV
28 mimic manganese oxides, and real-time reduction and oxidation rates can be calculated from
29 measured changes in the electric current over time. Alongside the electrodes, soil porewater
30 chemistry, pCO₂, pO₂, groundwater level, and precipitation were measured. Results indicate that
31 fixed-potential electrodes successfully detected temporally fine-scale fluctuations in metal redox
32 state, which was confirmed by the coordinated datasets. Water table fluctuations at the electrode
33 depth drove metal reduction, and rainfall events stimulated oxidation reactions in the vadose zone.
34 For the first time in soils, we directly measured the frequency, period, and amplitude of oxidation
35 and reduction events. All of these are key variables that control the biogeochemical impact of
36 metal oxide redox in terrestrial systems. At the SSHCZO we observed multi-day reduction or
37 oxidation events with a return interval of 5 – 10 days, controlled by precipitation frequency. Such
38 measurements with fixed-potential electrodes hold promise for accurately exploring the fast-
39 changing biogeochemical impacts of metal redox in upland soils where such reactions have been
40 difficult to quantify.

41

42 INTRODUCTION

43 Both iron (Fe) and manganese (Mn) are key to the biogeochemical cycling of carbon (C),
44 nutrients, and trace elements in soils (Borch et al. 2009; Henderson et al. 2012; Herndon et al.
45 2017; Ma et al. 2020). When soil O₂ concentrations are low, many soil bacteria readily switch to
46 Mn and Fe as alternate terminal electron acceptors for respiration (Lovley and Phillips 1988; Pett-
47 Ridge et al. 2006; DeAngelis et al. 2010). This microbially-mediated reduction mobilizes sorbed
48 and coprecipitated carbon, nutrients, and trace metals to porewaters for uptake or leaching to
49 groundwaters (Chacon et al. 2006; Buettner et al. 2014; Linkhorst et al. 2016). As soil pores
50 reoxygenate, the oxidation of both Fe and Mn may generate reactive intermediaries that serve an
51 important role in the decomposition of large and recalcitrant organic molecules like lignin (Hall
52 and Silver 2015; Jones et al. 2018).

53 Despite the importance of these metal redox reactions in soils, they are difficult to measure
54 *in situ* and the lack of field measurements limits our understanding of the impacts of Fe and Mn
55 redox changes on soil biogeochemistry. As of now, scientists use a range of active or passive
56 methods to track redox conditions in soils (Fiedler et al. 2007; Scott et al. 2021). Direct
57 measurement of redox potential (Eh) in soils with platinum tip electrodes is useful, but costly.
58 Additionally, measurements of redox potential by platinum electrodes are negatively impacted by
59 micro-scale heterogeneity, and do not provide data on specific redox reactions and rates
60 (Rabenhorst et al. 2009). To address some of the drawbacks of Eh probes, others use passive redox
61 probes of either Fe (Caell and Anderson 1986; Bridgman et al. 1991; Castenson and Rabenhorst
62 2006; Rabenhorst and Burch 2006; Owens et al. 2008; Hodges et al. 2018) or Mn (Dorau and
63 Mansfeldt 2015, 2016; Scott et al. 2021) to track the presence/absence of reducing or oxidizing
64 conditions relative to a specific redox couple over a set time period. Though they are inexpensive

65 and simple to use, these probes only provide an integrated measure of oxidizing and reducing
66 conditions over the weeks they are installed in the ground. Electrodes with redox-couple specificity
67 and real-time quantification of electron flux would allow for more complete exploration of the
68 frequency and periodicity of metal redox oscillations and therefore the biogeochemical importance
69 of metal redox in subsurface environments.

70 Recently, graphite electrodes fixed at a specific redox potential were used to track *in situ*
71 anaerobic microbial metabolisms in organic permafrost (Friedman et al. 2013) and riparian zones
72 known for methanogenesis (Friedman et al. 2016). These fixed-potential electrodes, long used by
73 electrochemists, can be used for chronoamperometry to measure the current produced at the
74 electrode surface over time. When set at environmentally relevant redox potentials, the recorded
75 currents indicate the real-time rate of electron flow into or out of the working electrode so that
76 negative currents correspond to oxidation and positive currents to reduction at the set potential.

77 Given the importance of metal redox cycling and the limitations of traditional redox
78 methods in soils, we sought to apply the method explored by Friedman et al. (2013) to track *in situ*
79 Fe and Mn redox reactions in upland mineral soils – the first deployment of such electrodes in
80 upland settings with lower soil moisture content. Our goal was to establish the efficacy of these
81 electrodes for tracking Fe and Mn redox in soils and demonstrate the seasonal metal redox cycling
82 at the Shale Hills watershed (Hodges et al. 2019a). Based on work reported in Hodges et al.,
83 (2019a), we hypothesize that metals become reduced during the late growing season when demand
84 for O₂ is high and soils are warm and wet. These reduced metals remain in small pore domains and
85 oxidize upon exposure to O₂ as soils dry the following spring. To test this hypothesis, we installed
86 graphite electrodes fixed at 100 mV (to mimic Fe oxides) and 400 mV (to mimic Mn oxides) at 50
87 cm and 70 cm belowground in a valley floor soil at the Susquehanna Shale Hills Critical Zone

88 Observatory (SSHCZO). The SSHCZO is ideal for this installation because it is an intensively
89 monitored watershed with well-documented seasonal and intermittent Fe and Mn redox cycling
90 driven by both abiotic and biotic reactions (Herndon et al. 2011; Yesavage et al. 2012; Herndon et
91 al. 2014; Kraepiel et al. 2015a; Hodges et al. 2019a). We also measured soil partial pressure of
92 carbon dioxide ($p\text{CO}_2$), partial pressure of oxygen ($p\text{O}_2$), groundwater level, and porewater
93 chemistry and used these corresponding data to interpret the currents we measured with the fixed-
94 potential electrodes.

95

96 Materials and Methods

97 *Susquehanna Shale Hills Site Description*

98 Measurements were focused at the south planar valley floor (SPVF; 40.66682 N, 77.9018
99 W) hillslope position in the Shale Hills catchment of the SSHCZO (Brantley et al. 2013, 2016,
100 2017). Shale Hills is an intensively monitored, 7.9 ha watershed in the Valley and Ridge
101 physiographic province of central Pennsylvania, USA. The catchment is underlain by the iron-
102 rich Rose Hill shale of the Silurian Clinton Formation, characterized by steep, planar slopes that
103 drain to an intermittent stream that flows from winter through mid-summer (Brantley et al.
104 2017). SPVF is adjacent to this stream and is monitored with nested lysimeters at 40 and 60 cm,
105 a groundwater monitoring well, and soil gas collection wells at 20, 40, and 120 cm.

106 The SPVF soil is mapped as a 120 cm deep Ultisol that is seasonally saturated at the
107 beginning of the growing season (Lin et al. 2006). Upslope of SPVF the soils become shallow
108 and well-drained Entisols over fractured shale. Previous work indicates a shallow preferential
109 flowpath for soil porewaters downslope over and through this fractured and weathered shale to

110 the subsurface of the SPVF soil, where porewaters converge with older, deeper
111 groundwaters.(Lin et al. 2006; Jin et al. 2011)

112

113 *Fixed Potential Electrode Installation and Analysis*

114 We installed graphite fixed-potential electrodes (10 x 2.5 x 0.6 cm dimensions) at 50 and
115 70 cm in the soil at SPVF in March 2019. At both depths we installed a three-electrode system
116 consisting of one working electrode, one counter electrode, and one reference electrode. The
117 graphite working electrode is in contact with the soil and is the point of electron transfer at a set
118 potential. The glass Ag/AgCl reference electrode in contact with the soil dictates the potential to
119 apply to the working electrode. The graphite counter electrode in contact with the soil, which is
120 identical to the working electrode in material and dimensions, completes the circuit with the
121 working electrode so that an electrochemical current between the working electrode and counter
122 electrode can be measured. Negative currents represent oxidation, that is electron flow out of the
123 electrode, at the set potential. Positive currents represent reduction, that is electron flow into the
124 electrode, at the set potential.

125 We chose 50 cm and 70 cm at SPVF because there are contrasting soil properties and soil
126 moisture conditions that we anticipated would lead to different redox conditions over the
127 growing season. The 50 cm electrodes are in a Bw horizon characterized by silty clay loam soil
128 texture and no redoximorphic features. The 70 cm electrodes were installed in the Bt horizon,
129 which is characterized by a silty clay texture and redoximorphic Fe concentrations and
130 depletions. In May 2019 we additionally installed three-electrode systems at 20 cm and 50 cm at
131 the south planar midslope (SPMS) above SPVF to provide an oxic contrast to SPVF. However,
132 that site was abandoned due to dry conditions in the late growing season that caused desiccation

133 of the reference electrodes and loss of contact of the working electrodes with the soil.
134 Desiccation was recognized by crystallization of the AgCl reference solution around the tip of
135 the reference electrode. The channels within the soil at SPMS limited contact with the soil, and
136 so it is reasonable to think that other well-drained soils with fewer coarse fragments would not
137 have the same limitations.

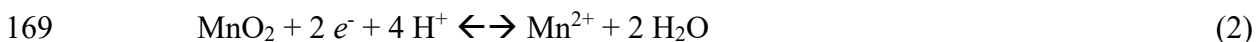
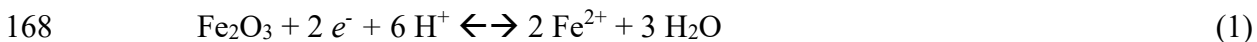
138 To install the electrodes, a hole was dug to match the diameter (40 cm) of a schedule 80
139 polyvinyl chloride (PVC) tube. Slots were cut in the PVC tube at 50 and 70 cm depth below the
140 soil surface so that the working, reference, and counter electrodes could be pushed through the
141 slots and into the soil. Slots for the reference electrodes were positioned within 1 cm of the
142 working electrodes, and counter electrodes were spaced about 4 cm from the working electrode.
143 The three electrodes were pushed into the soil so that approximately 3 cm remained out of the
144 soil. Graphite working and counter electrodes were installed so that the larger surface area was
145 perpendicular to the soil surface to prevent the potential for water ponding atop the electrodes.

146 Once installed, the tubes were capped and sealed to prevent atmospheric air and
147 precipitation from entering but remained open at the bottom contact with the soil. This setup
148 allowed for access to working and counter electrodes for refurbishment and replacement of
149 reference electrodes. The Ag/AgCl reference electrodes were checked monthly and replaced as
150 needed when no more reference solution remained in the glass body of the electrode.

151 Potentials at the graphite electrodes were poised using Nanoelectra Nev4 USB
152 potentiostats (Nanoelectra S.L. Madrid, Spain) connected to a field laptop (Latitude 5430
153 Rugged PC, Dell, Round Rock, Texas, USA), with current data collected every 30 s and stored
154 on the laptops. For analysis and data visualization, currents recorded by the potentiostats were
155 averaged every 12 minutes. Potentials were set at 100 mV relative to the standard hydrogen

156 electrode (SHE) to mimic the redox potential of Fe oxides (Fiedler et al. 2007). To complement
157 the 100 mV data, a second set of electrodes were installed in an adjacent tube at 50 and 70 cm at
158 SPVF in late April 2020 and fixed at 400 mV vs. SHE. This redox potential was chosen to
159 bracket the range of suboxic redox potentials in soil and to specifically mimic Mn oxides in the
160 soil environment (Fiedler et al. 2007).

161 From the measured currents, we calculated the oxidation and reduction rates at 100 mV
162 (in 2019 and 2020) and 400 mV (in 2020 only). For the electrodes at 100 mV, we calculated the
163 rate of the redox reactions in terms of Fe reduced or oxidized (Eq. 1). At 400 mV, we calculated
164 the rate of the redox reactions in terms of Mn reduced or oxidized (Eq. 2). Equations 1 and 2
165 represent reactions with example minerals (hematite and pyrolusite, respectively), but the fixed-
166 potential electrodes allow electron (e^-) transfer across a range of Fe and Mn (oxy)hydroxides
167 (Friedman et al. 2013; Logan et al. 2019).



170 The extent of metal reduction was calculated based on the integrated value of all positive
171 currents over the monitoring period ($Amps_{red}$), which were then divided by Faraday's constant
172 (F) to convert to moles of electrons transferred (e^-_{red}). Using the reaction stoichiometry (Eqs. 1,
173 2), the surface area of the electrodes in contact with the soil (SA , about 30 cm^2 but varies by
174 installation based measured length in contact with soil), and an estimate of the specific surface
175 area (SSA , $250,000 \text{ cm}^2 \text{ g}^{-1}$) of the bulk soil (Jin et al. 2010a) attributable to Fe (1% at 50 cm,
176 1.2% at 70 cm; Yesavage et al. 2012) or Mn (0.1% at 50 and 70 cm; Herndon et al. 2011;
177 Kraepiel et al. 2015b) oxides at SPVF, we calculated the total amount of Fe or Mn reduced over
178 the monitoring period in each season (Fe_{red} , Mn_{red} , eqs. 3, 4)

179 $\int Amps_{red} * F^{-1} * SA^{-1} * SSA * \frac{Fe}{e^-} = Fe_{red} (\text{mol g}^{-1})$ (3)

180 $\int Amps_{red} * F^{-1} * SA^{-1} * SSA * \frac{Mn}{2 e^-} = Mn_{red} (\text{mol g}^{-1})$ (4)

181 Oxidation extent was calculated similarly, instead based upon the integrated value of all negative
182 currents ($Amps_{ox}$) over the monitoring period (Eqs. 5, 6).

183 $\int Amps_{ox} * F^{-1} * SA^{-1} * SSA * \frac{Fe}{e^-} = Fe_{ox} (\text{mol g}^{-1})$ (5)

184 $\int Amps_{ox} * F^{-1} * SA^{-1} * SSA * \frac{Mn}{2 e^-} = Mn_{ox} (\text{mol g}^{-1})$ (6)

185 Where e^-_{ox} represents the moles of electrons transferred in the oxidation reactions, and Mn_{ox} and
186 Fe_{ox} represent the moles of Mn or Fe oxidized per g of soil, respectively.

187 We also calculated average rates of Mn and Fe oxidation and reduction per mass of soil
188 (\overline{r}_{ox} , \overline{r}_{red} , $\text{mol g}^{-1} d^{-1}$). For each monitoring period, we calculated the average positive or
189 negative currents and replaced the integrated current in equations 3 through 6 with that
190 calculated average.

191

192 *Concurrent Data Collection*

193 Soil porewater, pCO₂, pO₂, precipitation, and groundwater level were collected to
194 correspond with the fixed-potential electrode measurements made at SPVF. The soil porewaters
195 at SPVF and SPMS were collected with suction lysimeters specifically for dissolved Fe⁺² and
196 Fe^{tot} determination with the ferrozine assay (e.g., Viollier et al. 2000; Huang and Hall 2017). We
197 used hydroxylamine HCl to reduce all Fe in solution prior to the ferrozine assay to measure Fe^{tot}.
198 Absorbances were measured with a UV-Vis spectrophotometer (Biotek, ELx808 absorbance
199 reader, Agilent, Santa Clara, California, USA). Detection limit of this method is 1 uM Fe.
200 Samples were run in triplicate and concentration measurements were accepted if coefficient of

201 variation was less than 5%. Tensions of -50 kPa were set at the lysimeters and porewaters were
202 collected 1 hr afterward to limit the exposure of any potentially reduced Fe to atmospheric O₂.
203 All lysimeters were still sealed under vacuum at the 1 hr sampling point. While O₂ from within
204 soil may have interacted with collected porewaters, the vacuum and short time for samples to
205 draw was intended to limit the potential for oxidation of reduced Fe in porewaters. Samples were
206 immediately acidified to a pH of 2 with HCl to preserve the oxidation state of Fe in solution
207 (Stumm and Morgan 1996). All porewater samples were subsequently refrigerated prior to
208 analysis.

209 In 2019 soil pCO₂ and pO₂ measurements were made at the soil gas wells at SPVF.
210 Hasenmueller et al. (2015) summarized the installation procedure for the soil gas wells and Hodges
211 et al. (2019a) outlined the analysis procedure for pCO₂ and pO₂ data. Samplers were constructed
212 of stainless-steel tubing with stainless-steel mesh affixed to one end. Holes were augered to the
213 desired depth – in this case 20, 40, and 120 cm – and the samplers were placed in the hole. Sieved
214 coarse fragments from the soil were installed around the mesh end to facilitate air circulation and
215 then sieved < 2 mm soil was used to backfill the holes to limit the potential for vertical air
216 movement.

217 While sampling was attempted every 2 weeks, high soil moisture at times limited sampling
218 in May 2019 because the tubes were filled with water. Air-tight syringes with a one-way lock were
219 used to sample the gas tubes for pCO₂. All gas tubes were purged of 5 mL of gas in the 20 and 40
220 cm wells, and 10 mL of gas in all 120 cm wells to ensure sampling of soil atmosphere, and not
221 dead air in the tube. Immediately after purging, 5 mL of soil gas were collected with the locking
222 syringe for analysis in the laboratory. Afterward, 10 mL of soil gas were sampled for pO₂ using a
223 handheld soil gas analyzer (model 901, Quantek Instruments, Grafton, Massachusetts, USA). The

224 Quantek 901 has a range of 0 to 100% O₂ and an accuracy of $\pm 0.1\%$ O₂. As recommended by the
225 manufacturer, the Quantek is calibrated using O₂-free gas and ambient air every four years. Three
226 samples of ambient air were collected with locking syringes 30 cm above the ground surface per
227 hillslope position for ambient CO₂. Soil gas samples were analyzed in the laboratory on a flow-
228 through infrared gas analyzer (LI-7000, LiCOR Inc.) within two days of collection. Measurement
229 accuracy is within 1% of measured value.

230 The 2019 pCO₂ and pO₂ samples were assessed based on the 1 : -1 molar relationship
231 expected for aerobic carbohydrate respiration, corrected for gas diffusion as detailed in Angert et
232 al. (2015) and Kim et al. (2017). Results are presented in this paper in the same way as previous
233 publications reporting results from the SSHCZO (Hodges et al. 2019a, 2021). Briefly, the soil gas
234 data are plotted as pCO₂ vs. pO₂, relative to a line defined by a slope of -0.76 (the ratio of the two
235 diffusion constants) and an x-axis origin of 20.95% (the concentration of O₂ in the atmosphere).
236 When data deviate from this line, processes other than aerobic respiration of carbohydrates and
237 gas diffusion are affecting soil pCO₂ or pO₂. In this study, data falling above the theoretical line
238 indicate excess CO₂ in the soil pore gas compared to changes in O₂, and thus anaerobic respiration.
239 Additionally, for the purposes of this study, points below the theoretical line are consistent with
240 greater O₂ depletion relative to CO₂ in the soil system than predicted by the reaction stoichiometry,
241 i.e., chemolithoautotrophic oxidation.(Angert et al. 2015)

242 Because the gas wells at SPVF were often flooded in the sampling period of 2019, we
243 installed soil CO₂ and O₂ sensors at 50 and 70 cm at SPVF in March of 2020. Sensors can collect
244 soil gas data even under high soil moisture conditions and these depths provide clear insights
245 into the biotic and abiotic processes affecting soil CO₂ and O₂ at the depths of our fixed-potential
246 electrode measurements. Unfortunately, the O₂ sensors failed two months after installation, and

247 therefore we report only pCO₂ data collected in 2020. Soil pCO₂ at 50 and 70 cm in SPVF was
248 sensed by an optical electrode (Eosense, EosGP, Dartmouth, Nova Scotia, Canada), and was
249 recorded every 15 minutes. Data were recorded by a datalogger (CR1000X, Campbell Scientific,
250 Logan, Utah, USA).

251

252 *Electrical Resistivity Tomography*

253 Because soil moisture has been shown as a strong control on metal redox cycling in
254 upland soils, we used time lapse 3-D electrical resistivity tomography (3D ERT) to map changes
255 in soil moisture weekly from mid-May through the end of June 2020. An Iris Instruments
256 (Orleans, France) Syscal Pro sounding resistivity meter was used to record resistivity. Resistivity
257 electrodes were arrayed in a rectangle centered around the fixed potential electrodes at an
258 interval spacing of 1.5 m with 8 resistivity electrodes in the x direction (parallel to stream) and 6
259 in the y direction (perpendicular to the stream, going upslope). Data were imported into the Iris
260 Instruments Prosys II software where missing data and anomalously high data points were
261 removed. Res3D-Inv (Aarhus GeoSoftware, Aarhus Denmark) was used to create inversions of
262 resistivity datasets. These inversions provide 3-dimensional visualizations of estimated resistivity
263 at each measurement date. Since soil texture and structure were assumed to remain constant over
264 the sampling period, any change in resistivity corresponds with a change in soil moisture
265 conditions. Higher resistivity indicates relatively drier conditions and lower resistivity indicates
266 relatively wetter conditions (Michot et al. 2003; Samouëlian et al. 2005; Garré et al. 2011).

267

268 *Data Analysis*

269 Unless otherwise noted (e.g., 3D ERT datasets), all analyses, calculations, and data
270 visualizations were performed using Python (Gosset and Wright 2017). The pandas package
271 (McKinney 2010; The pandas team 2020) was used for data management, analysis, and quality
272 assurance. Data visualization was performed using the matplotlib (Hunter 2007) and seaborn
273 packages (Waskom 2021). The SciPy package was used for the calculation of rates and extents
274 of redox reactions (Virtanen et al. 2020).

275 Results

276 *Fixed-Potential Electrode Measurements*

277 The fixed-potential electrodes in 2019
278 and 2020 indicated periodic redox at 100 and
279 400 mV in the subsurface of SPVF (Figures 1,
280 2, and 3). In the Spring of 2019, data were
281 collected in the two-month period between
282 April and June. At 50 cm, negative currents (to
283 about -0.3 mA) were detected periodically, but
284 otherwise values remained at 0 (Figure 1). The
285 longest non-zero event at 50 cm in Spring 2019
286 lasted for about 3 days. Negative currents
287 represent movement of electrons out of the
288 electrodes (i.e., cathodic electrode response)
289 into the soil system and thus oxidation at 100
290 mV. At 70 cm, currents remained at 0 but
291 periodically became positive and reached a
292 peak of about 26.5 mA (Figure 1). There were
293 three reducing events at 70 cm that lasted from
294 one to three days and occurred every three to
295 five days in May 2019. Positive currents
296 represent a movement of electrons out of the soil and into the electrode (i.e., anodic response)

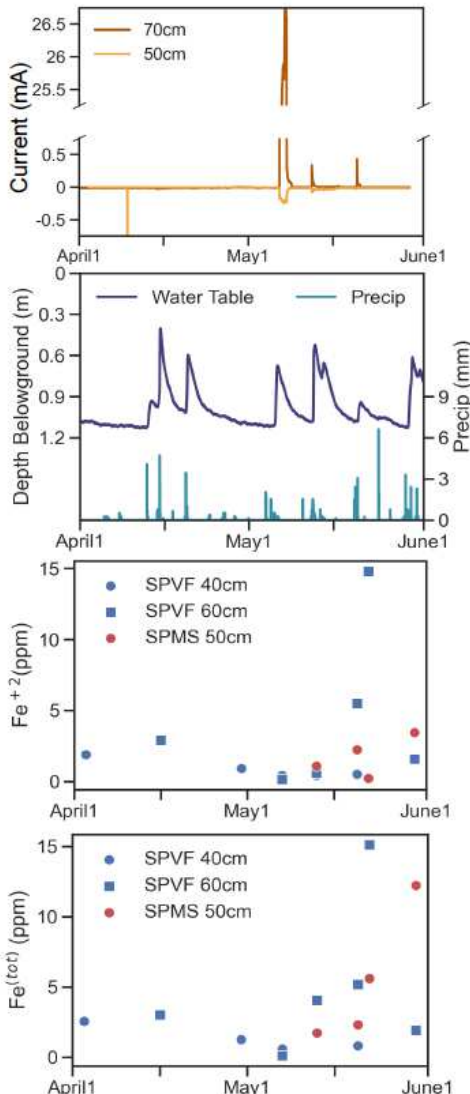


Figure 1. Data collected over the early growing season in 2019. From top to bottom, panels represent measured currents at the 50 cm and 70 cm 100 mV electrodes at SPVF, water table level and 10-min precipitation, Fe^{+2} concentrations in porewaters, and total Fe concentration in porewaters.

297 and thus represent reduction at 100 mV. The periodic negative currents at 50 cm and positive
298 currents at 70 cm co-occurred over the 2-month sampling period (Figure 1).

299 In 2019, data were also collected between September 15 and November 1. At 70 cm
300 currents remained at 0 mA throughout the monitoring period. At 50 cm, currents oscillate near 0
301 but occasionally become negative for periods of about 2 – 5 days, around -0.4 mA (Figure 2).

302 In 2020, data were collected in a two-month period between May and July (Figure 3).

303 Sampling dates were shifted one month later than 2019 because fixed potential-electrodes did not
304 detect measurable currents at 100 mV in April 2019. Here, we only present data visualizations of
305 the 70 cm electrodes, as currents measured at 50 cm remained around 0 mA throughout the
306 sampling period. In 2020, currents measured at the electrode fixed at 100 mV remain around -20
307 mA throughout the sampling period. On the other hand, currents measured at the electrode fixed
308 at 400 mV revealed variations between negative and positive currents from a low of around -100
309 mA in mid-May to a peak around 100 mA near the end of June (Figure 3-1).

310 From the fixed-potential electrode measurements in 2019 and 2020, we calculated the
311 average oxidation and reduction rates ($\overline{r_{ox}}$, $\overline{r_{red}}$) and the extent of oxidation/reduction ($Mn_{ox/red}$ &
312 $Fe_{ox/red}$) at 100 and 400 mV during the monitoring periods. In spring 2019, non-zero currents at
313 the 50 cm electrodes correspond to $Fe \overline{r_{ox}}$ of 1.9 mmol g⁻¹ d⁻¹ and an $Fe \overline{r_{red}}$ of 0 mmol g⁻¹ d⁻¹.
314 At 70 cm in spring 2019 $Fe \overline{r_{ox}}$ was 1.4 mmol g⁻¹ d⁻¹ and an $Fe \overline{r_{red}}$ of 108 mmol g⁻¹ d⁻¹. Activity
315 at the electrodes correspond to an Fe_{ox} of 0.98 mmol Fe kg⁻¹ and an Fe_{red} of 2.7 mmol Fe kg⁻¹ at
316 50 cm, and Fe_{red} of 39 mmol Fe kg⁻¹ and an Fe_{ox} of 0.67 mmol Fe kg⁻¹ at 70 cm. The average

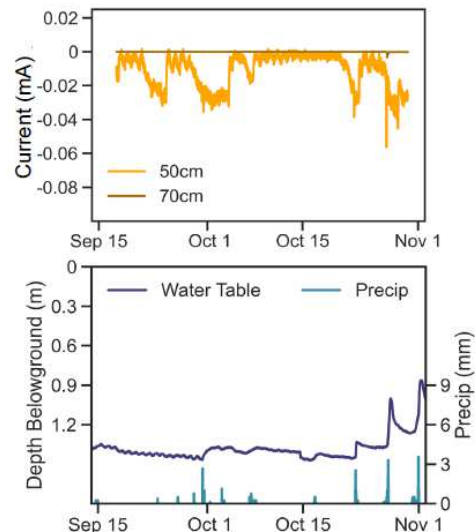
317 rates and extent of Fe reduction or oxidation
318 account for the 2-month monitoring period at the
319 beginning of the 2019 growing season.

320 In Fall 2019, currents at the 70 cm electrode
321 remained around 0 mA throughout the monitoring
322 period, but there were oxidizing events at 50 cm
323 (Figure 2). Over this sampling period the measured
324 currents correspond to an $Fe \overline{r_{ox}}$ of $1.3 \text{ mmol g}^{-1} \text{ d}^{-1}$
325 and an Fe_{ox} of $0.58 \text{ mmol Fe kg}^{-1}$.

326 In 2020, we observed no activity at the
327 sensors at 50 cm, but a strong signal of oxidation at
328 100 mV and oscillations between oxidation and
329 reduction at 400 mV. Also, in comparison to 2019,
330 the currents produced were of a greater magnitude in 2020. Non-zero currents at the 100 mV 70
331 cm electrodes correspond to $Fe \overline{r_{ox}}$ of $2 \text{ mol g}^{-1} \text{ d}^{-1}$ and an Fe_{ox} of $0.75 \text{ mol Fe kg}^{-1}$. At the 400
332 mV electrodes, $Mn \overline{r_{ox}}$ was $0.19 \text{ mmol g}^{-1} \text{ d}^{-1}$ and an $Mn \overline{r_{red}}$ of $0.15 \text{ mmol g}^{-1} \text{ d}^{-1}$. Activity at
333 these electrodes correspond to an Mn_{red} of $34 \text{ mmol Mn kg}^{-1}$ and an Mn_{ox} of $15 \text{ mmol Mn kg}^{-1}$.
334

335 *Water Table and Precipitation*

336 In general, soils were wetter in Spring 2019 than in Spring 2020 (Figures 1, 3), while
337 average air temperatures, which increased from around 8°C in April to 22°C in July, were about
338 the same in 2019 and 2020. In 2019 precipitation events were frequent between April and June
339 with a total of about 23 cm of rain falling in the 61-day period. This precipitation caused water



326 **Figure 2.** Data collected over the late
327 growing season in 2019. The top panel
328 represents measured currents at the
329 50cm and 70 cm 100 mV electrodes,
330 and the bottom panel represents water
331 table level and 10-min precipitation.
332 Soils were too dry to produce porewater
333 samples for Fe analysis.

340 table fluctuations up to and above the sensors installed at 50 and 70 cm. In Fall 2019, about 15
341 cm of rain fell in the 65-day period. The water table level rose after precipitation events and
342 reach a minimum of 90 cm below the soil surface by the end of the monitoring period (Figure 2).
343 From May through June 2020, precipitation was infrequent and half the volume of precipitation
344 in Spring 2019 (10 cm). This infrequency of precipitation caused the water table to remain below
345 1 m through most of the 2-month period (Figure 3).

346

347 *Porewater Chemistry*

348 We measured the concentration of Fe^{2+} and Fe^{tot} ($\text{Fe}^{2+} + \text{Fe}^{3+}$) in porewaters at 40 cm and 60 cm
349 at SPVF and upslope of SPVF (SPMS) at 50 cm over the sampling periods in 2019 and 2020. In
350 general, concentrations of Fe^{2+} and Fe^{tot} remained below 5 ppm throughout both the 2019 and 2020
351 growing seasons (Figures 1 and 3).

352 In 2019, porewater Fe^{2+} concentration peaked towards the end of May at 15 ppm at the 60 cm
353 SPVF lysimeter, while porewater Fe concentrations remained below 3 ppm at 40 cm. Additionally
354 at both 40 and 60 cm in SPVF, Fe^{2+} and Fe^{tot} were about the same concentration in each sample.
355 This indicates that most dissolved Fe was Fe^{2+} . At SPMS, samples were difficult to collect due to
356 dry conditions, but the samples that were collected indicated an increase in Fe^{tot} concentrations
357 from about 2 ppm in the middle of May to 12 ppm at the beginning of June. Unlike SPVF, the
358 samples from SPMS showed $\text{Fe}^{2+} < \text{Fe}^{\text{tot}}$, indicating a greater proportion of dissolved oxidized iron
359 at SPMS than SPVF.

360 Porewaters collected in 2020 indicated low Fe concentrations (< 5 ppm) at both SPMS and
361 SPVF throughout much of the sampling period (Figure 3). The maximum recorded Fe^{2+} and Fe^{tot}
362 concentrations of about 8 ppm Fe^{2+} and 25 ppm Fe^{tot} were collected from the 40 cm SPVF

363 lysimeter at the beginning of June. All other samples collected from both SPVF and SPMS did not
364 show such a difference between concentrations Fe^{+2} and Fe^{tot} , indicating that most Fe in solution
365 was reduced.

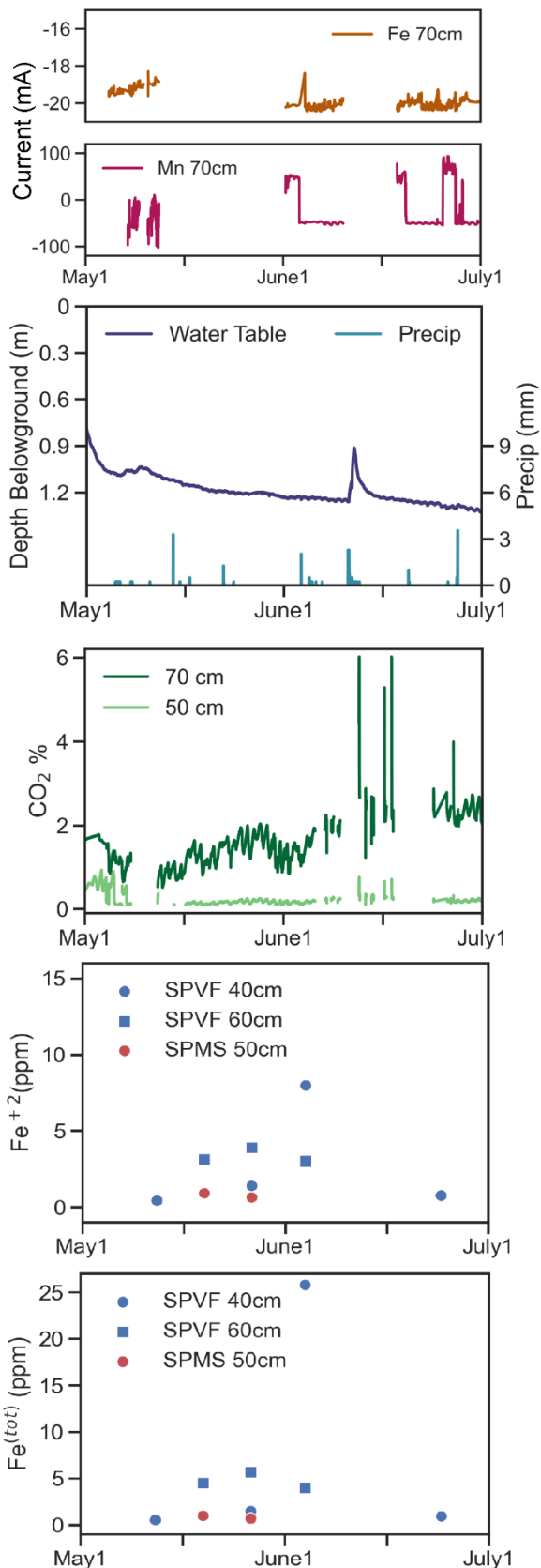


Figure 3. Data collected over the early growing season in 2020. From top to bottom panels represent measured currents at the 70 cm 100 and 400 mV electrodes, water table level and 10-min precipitation, sensor-measured CO₂ concentrations at 50 and 70 cm, Fe⁺² concentrations in porewaters, and total Fe concentration in porewaters.

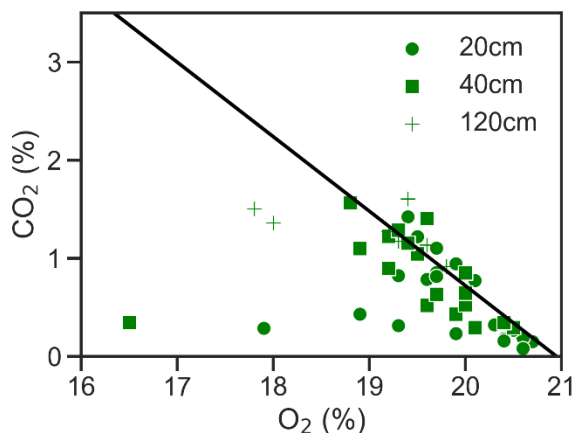


Figure 4. Soil pCO₂ and pO₂ measured at SPVF from 20 cm, 40 cm, and 120 cm gas wells. Different symbols represent data from different soil depths. The black line represents the theoretical relationship of soil pCO₂ vs. pO₂ given aerobic respiration on a carbohydrate substrate and gas diffusion.

Soil Gases

In 2019, soil pCO₂ and pO₂ were hand-sampled between April and June. Sampling was attempted at 20, 40, and 120 cm, but few samples were obtained from 120 cm due to inundated gas wells. The collected samples indicated that aerobic respiration and diffusion are the prevailing controls on the two gases because the data mostly plot along the line representing

378 aerobic respiration and diffusion (Figure 4). However, there are some points, most notably
 379 sampled from 20 cm and 40 cm, that fall well-below the line representing the stoichiometry
 380 between pCO₂ and pO₂ expected when aerobic respiration and gas diffusion are the dominant
 381 processes.

382 In 2020, soil pCO₂ was sensed and recorded at 15-minute intervals from the beginning of
 383 May through mid-July at 50 and 70 cm, the depths of the fixed-potential electrodes (Figure 3).
 384 Throughout the monitoring period, soil pCO₂ was higher at 70 cm than at 50 cm. At 70 cm soil
 385 pCO₂ was lowest at the beginning of May, around 1%, and increased to vary around 2% in July.
 386 There were additional periodical peaks, some to above 6%, at 70 cm. Contrasting with 70 cm, 50
 387 cm soil pCO₂ was highest around the beginning of May and remained below 1% throughout the
 388 rest of the monitoring period.

390 *Soil 3D ERT in 2020*

391 In 2020 we used weekly 3D ERT measurements to track the change in soil moisture
392 conditions around the fixed-potential electrodes from May 20 through June 24. We present
393 inversions (i.e., estimates of subsurface resistivity) of the apparent resistivity measurements
394 along both the X-Y and X-Z axes. When examining resistivity along the X-Y axis such that each
395 slice represents conditions at a single depth, it is clear that resistivity was higher, and therefore
396 soil moisture was lower, at 50 cm than it was at 70 cm (Figure 5). In the panels of Figure 5, the
397 100 mV electrodes are located at $x = 2.5$ m, $y = 1.5$ m, and the 400 mV electrodes at $x = 1.25$ m,
398 $y = 1.5$ m. At 50 cm, the resistivity around the electrodes was above $250 \Omega * m$ for most of the 6-
399 wk monitoring period. At 70 cm resistivity was consistently lower, around $150 \Omega * m$. Although
400 differences in depth are apparent over these dates, there was not much change in resistivity over
401 the 6 wks.

402 This lack of change in resistivity (and therefore soil moisture) over time from May 20,
403 2020 through June 24, 2020 is clear when examining slices along the X-Z axis located at the
404 point along the y axis where the electrodes were installed (Figure 6). In these slices, the 400 mV
405 electrodes are located at $x = 1.25$, $z = 50, 70$; and the 100 mV electrodes are located at $x = 2.5$, z
406 = 50, 70. In addition to the lack of change in resistivity over time in these soils, it also appears
407 that there was a zone of higher resistivity centered around the area that the 100 mV electrodes
408 are installed compared to the 400 mV electrodes.

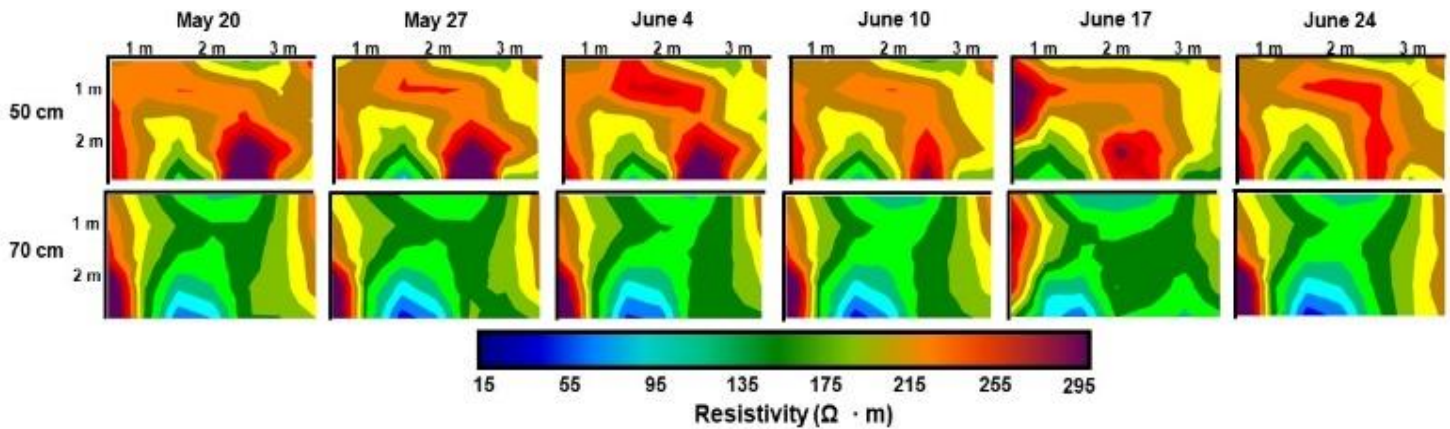


Figure 5: Soil ERT slices along the X-Y axis from the weekly measurements in 2020. These slices represent the change of resistivity at a single depth over time centered around the fixed-potential electrodes. The top row represents resistivity at 50 cm, and the bottom row resistivity at 70 cm. The bottom of each plot is towards the stream, and the top of each plot is oriented upslope. Warm colors represent higher resistivity and therefore dryer conditions, cool colors represent lower resistivity and wetter conditions.

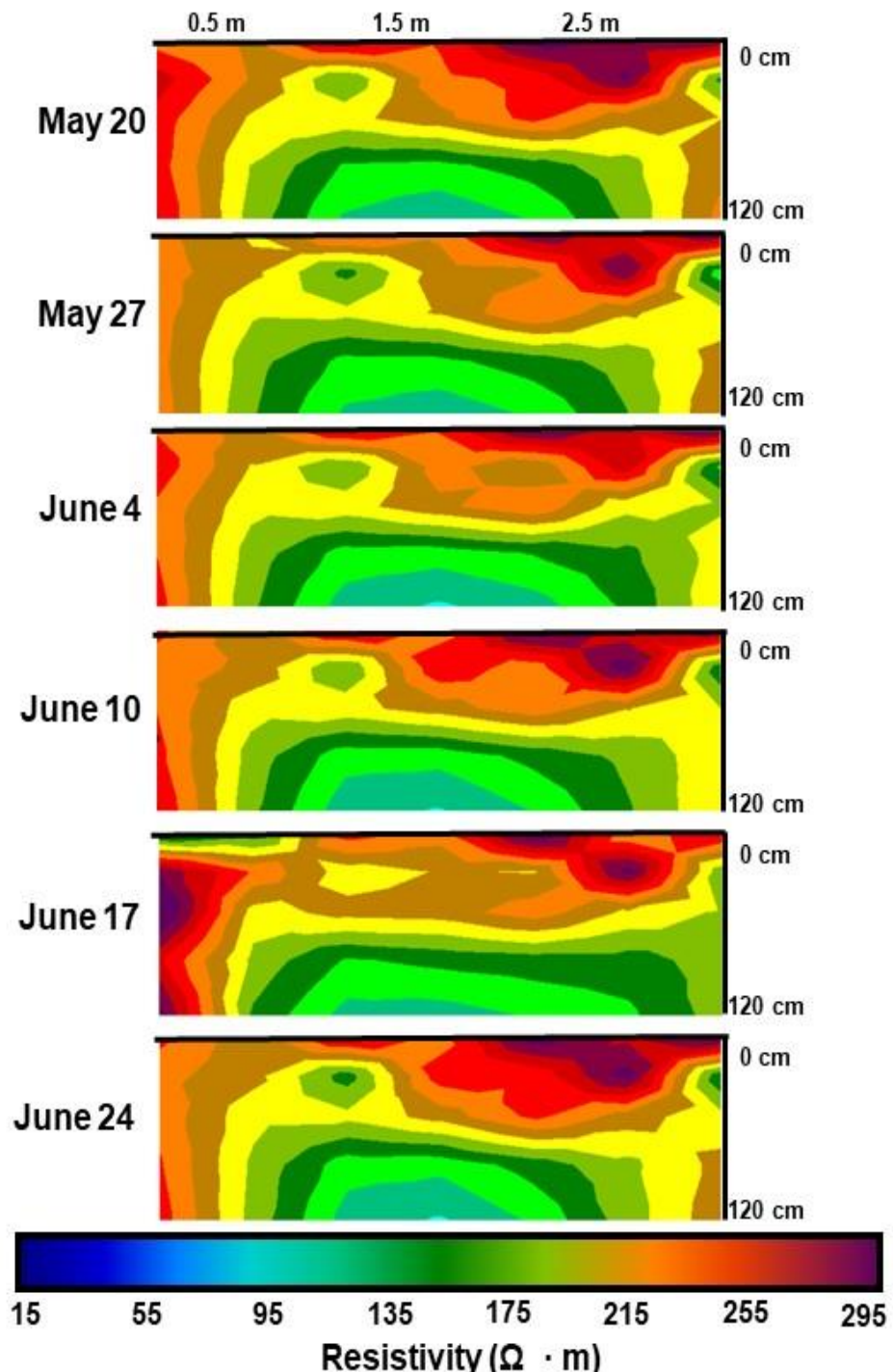


Figure 6: Soil ERT slices along the X-Z axis from the weekly measurements in 2020. These slices represent the change of resistivity with depth in the soil profile and over time centered around the fixed-potential electrodes. The 400 mV electrodes are installed at 1 m and the 100 mV at 2.5 m along the X axis. Warm colors represent higher resistivity and therefore dryer conditions, cool colors represent lower resistivity and wetter conditions.

411 Discussion

412 Our data show, for the first time, the *in situ* dynamics of metal redox in upland mineral
413 soils. While a pilot-scale study with low replication, the fixed-potential electrodes allowed for
414 the observation of rate, amplitude, period, and frequency of redox events in the early and late
415 growing season of an upland soil. The corresponding water table, precipitation, porewater
416 chemistry, soil pCO₂, and 3D ERT data contextualize the currents from the fixed-potential
417 electrodes and point to the importance of soil moisture and demand for O₂ for respiration in
418 sustaining redox cycling in uplands. Below we discuss the redox dynamics observed at SPVF,
419 the spatial heterogeneity of those redox reactions elucidated from the 3D ERT measurements, the
420 apparent controls of soil moisture on metal redox at Shale Hills, and the significance of our work
421 in the context of the roles that metal oxides play in the biogeochemical functioning of upland
422 soils.

423

424 *Fixed-Potential Electrodes Capture in situ Redox Dynamics*

425 The results from SPVF show redox fluctuations between negative and positive currents at
426 both 100 mV and 400 mV, and therefore indicate active redox cycling of both Fe and Mn. The
427 only known previous installations of fixed-potential electrodes documented smaller magnitude
428 positive currents in thawing permafrost soils where Fe reduction is known to account for over
429 half of soil respiration, (Lipson et al. 2010; Friedman et al. 2012, 2013) or in riparian zones with
430 active methanogen populations (Friedman et al. 2016). Our results show that fixed-potential
431 electrodes are useful for documenting redox dynamics (not just reducing conditions) in
432 moderately well-drained upland soils that may not be predominantly reducing. From our results
433 and those reported by Friedman et al. (2012, 2013, and 2016) fixed-potential electrode

434 measurements can be applied to a diverse array of soils (permafrost soils, riparian floodplain
435 soils, and upland soils) to document reduction *and* oxidation reactions across a range of redox
436 potentials.

437 Our findings provide novel insights into the temporal dynamics of the documented Fe
438 and Mn redox cycling and anaerobic respiration in the soils of Shale Hills. For example,
439 Yesavage et al. (2012) found evidence of Fe reduction and subsequent oxidation through
440 calculations of Fe enrichment and depletion relative to the shale parent material, presence of Fe
441 cycling bacteria, and Fe isotope ratios. This paper proposed two mechanisms of Fe fractionation
442 to explain the isotopically light Fe observed in the soils at SPVF: Fe fractionation upon reductive
443 dissolution in ridgeline and midslope soils with no fractionation upon reprecipitation as
444 secondary Fe oxides at the valley floor, or no fractionation upon mobilization upslope with
445 fractionation upon precipitation as Fe oxides. Our fixed-potential electrode results of fast Fe
446 redox cycling at SPVF, and little redox activity at the midslope, support mechanism 2, where
447 mobilized colloidal or organically-bound Fe is not isotopically distinct from the source rock, is
448 transported to the valley floor, and subsequently fractionates upon precipitation as Fe oxides
449 (Yesavage et al. 2012).

450 Furthermore, Herndon et al. (2011, 2014) and Kraepiel et al. (2014) documented active
451 Mn cycling facilitated by tree uptake. Roots take up reduced Mn that has been mobilized by
452 reductive dissolution; reduced Mn from this initial uptake is eventually deposited on the soil
453 surface in leaf litter. As that leaf litter decomposes and moves deeper in the soil profile, the Mn
454 in the litter becomes more oxidized. Our results show that this Mn enrichment relative to bedrock
455 results in a pool of soil Mn that undergoes fast rates of redox cycling. Finally, Hodges et al.
456 (2019), using soil pCO₂ and pO₂ measurements distributed across the Shale Hills watershed,

457 found evidence of seasonal metal redox cycling throughout the watershed, with the most
458 pronounced patterns at SPVF. Our results of consistent oxidation (i.e., only negative currents) in
459 Spring of 2020 support this hypothesis.

460 The fixed-potential electrode data also add a spatial element to the temporal dynamics
461 documented by Hodges et al. (2019a) by representing differences in redox cycling by depth at
462 any given time. Furthermore, the frequency and amplitude of the reducing and oxidizing events
463 during the three monitoring periods adds key real-world parameters that can be used for future
464 work constraining the biogeochemical importance of metal redox oscillations in soils. For
465 example, there is a broad set of literature in which the period and frequency of oxidizing and
466 reducing conditions is manipulated in order to investigate the biogeochemical and mineral
467 changes brought about by such fluctuating conditions (Thompson et al. 2006; Ginn et al. 2017;
468 Barcellos et al. 2018a). Future manipulated experiments may be improved if informed by the *in*
469 *situ* period and frequency of redox fluctuations recorded by fixed-potential electrode
470 measurements, like the ones presented in this work.

471 Our results add to the growing literature documenting anaerobic respiration in upland
472 soils that are not saturated with the frequency that was once thought to be necessary for metal
473 reduction (Hall et al. 2016; Barcellos et al. 2018b; Baish and Schaetzl 2021). Anaerobic
474 respiration has long been regarded as potentially important in upland soils (e.g., Sexstone and
475 Parkin 1985; Parkin 1987; Zausig et al. 1993; Lee et al. 1999; Verchot et al. 2000), but our
476 results are the first, to our knowledge, to measure *in situ* rates of anaerobic respiration with Fe
477 and Mn as a terminal electron acceptor within uplands. Furthermore, in 2020, our findings of
478 positive currents at 400 mV (indicating reduction at 400 mV) with water table levels well-below
479 70 cm capture low-oxygen processes in an upland soil with fine temporal resolution; our results

480 show that anaerobic respiration under unsaturated conditions can be maintained for multiple
481 days.

482 Precipitation events stimulated aerobic respiration, evidenced by increased pCO₂, and the
483 high demand for O₂ for respiration outpaced supply and subsequently resulted in reduction at 400
484 mV. These results of Mn reduction at Shale Hills mirror those of Warinnier et al. (2020) who
485 documented reductive dissolution of Mn in an unsaturated agricultural soil in France. Warinnier
486 et al. (2020) noted the importance of labile OC in stimulating respiration and causing the shift to
487 alternate terminal electron acceptors, like Mn. Though not measured in our study, infiltrating
488 precipitation delivers DOC to the subsurface at the SSHCZO (Andrews et al. 2011), which likely
489 further stimulated respiration in soils.

490 The fixed-potential electrodes indicate high average Fe reduction rates (1.7 mmol Fe g⁻¹
491 d⁻¹ at 70 cm in 2019) compared to the limited published data from other subsurface soils in
492 upland temperate watersheds. For example, during the spring in an upland soil in the piedmont of
493 South Carolina, USA Fe_{red} – calculated by change in HCl-extractable Fe⁺² over two weeks – at
494 60 cm was 0.02 mmol Fe kg⁻¹ d⁻¹, which is orders of magnitude lower than the rate we recorded
495 at SPVF (Hodges et al. 2019b). The temporal resolution of our measurements allows us to
496 measure the actual rates of reaction, which are flashy and difficult to resolve by measuring
497 change in concentration of reduced species. Because both oxidation and reduction occurred at all
498 the depths we monitored, measuring changes in reduced or oxidized species at weekly or
499 monthly intervals may indicate little to no net active redox, when in reality there may have been
500 multiple oscillations between oxidizing and reducing conditions. In general, the soils of SPVF
501 are oxidizing most of the time and become reducing in response to precipitation or water table
502 rise for less than 10% of the monitoring periods.

503 Porewater chemistry is consistent with the high Fe reduction rates calculated from the
504 fixed potential electrodes in 2019. While the baseline concentrations of 1 to 2 ppm Fe^{+2} and Fe^{tot}
505 in the soil solution at SPVF is comparable to average conditions in other temperate forests (Fuss
506 et al. 2010; Schaetzl and Rothstein 2016), the peaks in Fe^{+2} around 15 to 25 ppm are more like
507 the measured porewater concentrations of 18 ppm Fe^{tot} in freshwater marsh soils of Virginia,
508 USA (Chambers and Odum 1990) and the 20 ppm Fe^{+2} reported for wetland soils in a headwater
509 catchment in Bavaria (Knorr 2013). The high rate of Fe reduction and the high Fe^{+2}
510 concentrations in porewaters at Shale Hills are reflective of the high concentration of Fe in the
511 parent material of Shale Hills, but also point to the significance of Fe redox to biogeochemical
512 cycling at the site (Jin et al. 2010b; Yesavage et al. 2012)

513 The fixed-potential electrodes generate temporally explicit data that allow for a
514 mechanistic understanding of the drivers of metal redox in upland soils. For example, in 2019 we
515 found that Fe redox corresponded directly to water table fluctuations and rainfall events within
516 one to two days of the start of the event. This result signifies the importance of soil moisture to
517 the creation of low-oxygen conditions by limiting O_2 diffusion, and the movement of soil waters
518 in supplying electron acceptors or donors (Zausig et al. 1993; De-Campos et al. 2012). On the
519 other hand, in the Fall of 2019, oxidation events at 50 cm corresponded directly to precipitation
520 events. Oxygen-charged rainwaters likely stimulated oxidation of Fe in previously dry soils as
521 they percolated through SPVF.

522 In 2020, temporally explicit data indicated that precipitation events likely increased soil
523 respiration (evidenced by an increase in pCO_2 after precipitation), which in turn corresponded to
524 an increase in reduction at the 400 mV electrode at 70 cm. The electrodes demonstrated that this
525 reduction at 400 mV in 2020 was more or less balanced by subsequent oxidation. In this case,

526 hand-sampled pCO₂ and pO₂ may only indicate aerobic respiration because the CO₂ generated
527 without consumption of O₂ through anaerobic respiration would be balanced by the consumption
528 of O₂ through oxidation of Mn without production of CO₂. Such observations point to the value
529 of *in situ* real time measurements to observe redox fluctuations in soils.

530

531 *3D ERT Reveals Importance of Soil Morphology to Spatial Distribution of Redox Conditions*

532 While the 3D ERT established the soil moisture conditions surrounding the electrodes
533 over the monitoring period in 2020, it also represents the spatial heterogeneity of the soils of
534 SPVF. Even though aboveground the 100 mV and 400 mV electrodes are separated by about a
535 meter and are at the same hillslope position, the 3D ERT indicates that the 100 mV electrodes
536 were measured consistently higher resistivity conditions than the 400 mV electrodes. This
537 relatively higher resistivity could represent dense tree roots or a greater proportion of rock
538 fragments relative to soil in that region (Garré et al. 2011; Carrière et al. 2020).

539 These differences in soil conditions, in part, could explain why there was a consistently
540 negative current at 100 mV (representing oxidation of Fe), while the 400 mV electrode
541 fluctuated often between negative and positive currents (representing Mn reduction-oxidation
542 cycling). We expected that the 400 mV electrode would indicate oxidizing and reducing
543 conditions more frequently than the 100 mV in an upland soil because 400 mV is higher on the
544 “redox ladder” once O₂ is depleted (Fiedler et al., 2007). However, over periods of prolonged
545 positive currents at 400 mV, 100 mV still only measured as oxidizing at a negative current. A
546 soil with more coarse fragments, as suggested by the 3D ERT, could explain this departure from
547 expectations. A rockier soil would have higher macroporosity that would facilitate both drainage
548 of porewaters and diffusion of O₂ from the surface (Renault and Stengel 1994).

549

550 *The Role of Precipitation, Soil Moisture, and Water Table Fluctuations in Metal Redox at SPVF*

551 As established by previous work at Shale Hills (Hodges et al. 2019a) and in other humid,
552 temperate systems (Fuss et al. 2010; Knorr 2013; Hodges et al. 2019b), our study clearly
553 demonstrates the role of soil moisture in generating reducing conditions in upland soils. The
554 difference in redox activity between 2019 and 2020 can be explained by the differences in water
555 table level between the two years. In 2019 there was more precipitation and the water table
556 fluctuated between 100 and 50 cm belowground throughout the 2-month monitoring period,
557 while in 2020 there was less precipitation and the water table mostly remained below 100 cm.
558 Consequently, in 2019, we observed redox activity at both the 50 and 70 cm electrodes set at 100
559 mV. In 2020 there was no activity at 50 cm; at 70 cm we recorded only oxidation at the 100 mV
560 electrode and fluctuating currents at the 400 mV electrode. We would anticipate reduction at 400
561 mV before reduction at 100 mV, due to the differences in thermodynamic favorability (Fielder et
562 al., 2007). Therefore, these 2020 results point to less-reducing soil conditions due to lower soil
563 moisture in 2020 than in 2019. The prolonged oxidation we recorded at 100 mV in Fall 2020
564 supports our hypothesis that reduced species remain in porewaters over the late Fall and Winter,
565 and then are a sink for diffusing O₂ as soils dry in the Spring and Summer.

566 Clearly, soil moisture played a key role in sustaining the low-oxygen concentrations
567 necessary for reducing conditions, especially at the 100 mV redox potential. However,
568 precipitation events and the fluctuating water table also likely play a role in the delivery of
569 terminal electron acceptors and electron donors to the subsurface of SPVF. Others at Shale Hills
570 have developed a conceptual model of subsurface lateral flow paths that deliver precipitation that
571 infiltrates the hillslopes of Shale Hills and flows to the subsurface of the valley, including SPVF

572 (Lin et al. 2006; Jin et al. 2011; Yesavage et al. 2012). This zone of mixing of relatively young
573 lateral flow with the older regional groundwater is within the B horizon of SPVF. Porewater
574 chemistry from SPMS in 2019 (Figure 1) suggests that this lateral flowpath may have delivered
575 colloidal or organically-bound Fe³⁺ from the well-drained ridgeline and midslope soils to the
576 subsurface of SPVF, where it was subsequently reduced at the 70 cm electrode. Then, the rising
577 water table delivered Fe⁺² in the groundwater to the 50 cm electrode, where it was oxidized upon
578 exposure to O₂. From these dynamics of Fe reduction at 70 cm and oxidation at 50 cm, it appears
579 that in the early growing season of 2019, there was a redox transition zone in the B horizon of
580 SPVF.

581 Such redox transition zones have been demonstrated as key to the decomposition of large
582 organic molecules in the soil subsurface. For example, the oxidation of Mn²⁺ to the reactive
583 intermediate Mn³⁺ facilitates the oxidation of lignin and other particulate organic carbon at the
584 oxic/reduced interface of soils and sediments (Jones et al. 2018). Similarly, the oxidation of Fe²⁺
585 to form reactive hydroxyls and other O species through Fenton reactions is a mechanism of
586 decomposition of OC in soils with fluctuating redox conditions (Hall and Silver 2013). Fixed-
587 potential electrodes installed in such transition zones, along with coordinated observations, could
588 further elucidate the timing and significance of Mn and Fe oxidation to the decomposition of
589 recalcitrant organic molecules in the soil subsurface.

590

591 *Significance and Conclusions*

592 Our results provide reaction-specific confirmation of the seasonal Fe and Mn redox
593 cycling hypothesis for the Shale Hills Watershed (Hodges et al. 2019a). The fixed-potential
594 electrode measurements indicated predominant oxidation of reduced Fe in porewaters during the

beginning of the growing season. For the first time, we demonstrate that fixed-potential electrodes may be used to track *in situ* redox fluctuations in upland soils. These measurements likely provide the most accurate real-time rates of specific redox reactions in subsurface environments. Indirect measures like Eh electrodes, passive electrodes, dyes, and infrequent measurements of reduced species in porewaters are the most common methods for tracking anaerobic respiration and reducing conditions in soils (Castenson and Rabenhorst 2006; Rabenhorst et al. 2009; Stiles et al. 2010; Dorau and Mansfeldt 2016; Hodges et al. 2018). Fixed-potential electrodes are a useful complement to such methods so that rather than redox *potential*, actual redox reactions are quantified, given the substrates available *in situ*.

In addition to serving as important indicators of the drainage status of a soil, Fe and Mn redox often control the fate and biogeochemical cycling of C, P, and trace metals in soils and sediments. Arrays of fixed-potential electrodes, when coupled with environmental monitoring of dissolved C and other constituents, could better constrain the spatial and temporal dynamics of such reactions. Furthermore, electrodes fixed at other redox potentials in soils could provide real-time rates of denitrification, sulfate reduction, or methanogenesis. Studies of reductive dissolution and subsequent mobilization of metal oxide coprecipitates, oxidative decomposition of organic carbon by reactive intermediaries, and use of alternate terminal electron acceptors in soils could benefit from the data provided by fixed-potential electrode arrays.

613

614 ACKNOWLEDGMENT

Financial Support was provided by National Science Foundation grant EAGER SITS -1841568 to SLB, National Science Foundation Grant EAR – 1331726 (SLB) for the Susquehanna Shale Hills Critical Zone Observatory, United States Department of Agriculture Grant #2020-67034-31716 to

618 CH. Logistical support and/or data were provided by the NSF-supported Susquehanna Shale Hills
619 Critical Zone Observatory. This research was conducted in Penn State's Stone Valley Forest,
620 which is funded by the Penn State College of Agriculture Sciences, Department of Ecosystem
621 Science and Management and managed by the staff of the Forestlands Management Office. The
622 authors thank Jeremy Harper for assistance in the field and Brosi Bradley for field and laboratory
623 assistance.

624

625 **STATEMENTS & DECLARATIONS**

626 **Funding Sources**

627 NSF EAR – 1331726 to SLB, NSF EAGER SITS -1841568 to SLB, and USDA NIFA #2020-
628 67034-31716 to CH.

629 **Competing Interests**

630 The authors have no relevant financial or non-financial interests to disclose.

631

632 **Author Contributions**

633 All authors contributed to the study conception and design. Caitlin Hodges, Brandon Forsythe,
634 and David Oakley collected the electrode and resistivity measurements. Data analysis and the
635 first draft of the manuscript were completed by Caitlin Hodges. All authors commented on and
636 contributed to previous versions of this manuscript. All authors read and approved the final
637 manuscript.

638

639 **Data Availability**

640 All water table depth, soil gas concentration, precipitation, electrical resistivity tomography, and
641 soil moisture datasets are publicly available at www.czo.psu.edu.

642

643 REFERENCES

- 644 Andrews DM, Lin H, Zhu Q, et al (2011) Hot Spots and Hot Moments of Dissolved Organic
645 Carbon Export and Soil Organic Carbon Storage in the Shale Hills Catchment. *Vadose Zone Journal*. <https://doi.org/10.2136/vzj2010.0149>
- 647 Angert A, Yakir D, Rodeghiero M, et al (2015) Using O₂ to study the relationships between soil
648 CO₂ efflux and soil respiration. *Biogeosciences* 12:2089–2099.
649 <https://doi.org/10.5194/bg-12-2089-2015>
- 650 Baish CJ, Schaetzl RJ (2021) New insights into the origin and evolution of gossic features in
651 coarse-textured soils in northern lower Michigan (USA). *Soil Sci Soc Am J*.
652 <https://doi.org/10.1002/saj2.20331>
- 653 Barcellos D, Cyle KT, Thompson A (2018a) Faster redox fluctuations can lead to higher iron
654 reduction rates in humid forest soils. *Biogeochemistry* 137:367–378.
655 <https://doi.org/10.1007/s10533-018-0427-0>
- 656 Barcellos D, O'Connell CS, Silver W, et al (2018b) Hot Spots and Hot Moments of Soil Moisture
657 Explain Fluctuations in Iron and Carbon Cycling in a Humid Tropical Forest Soil. *Soil Syst*
658 2:59. <https://doi.org/10.3390/soilsystems2040059>
- 659 Borch T, Kretzschmar R, Kappler A (2009) Biogeochemical redox processes and their impact on
660 contaminant dynamics. *Environmental Science & Technology* 44:.
661 <https://doi.org/10.1021/es9026248>
- 662 Brantley S, DiBiase R, Russo T, Shi Y (2016) Designing a suite of measurements to understand
663 the critical zone
- 664 Brantley SL, Holleran ME, Jin L, Bazilevskaya E (2013) Probing deep weathering in the Shale
665 Hills Critical Zone Observatory, Pennsylvania (USA): the hypothesis of nested chemical
666 reaction fronts in the subsurface. *Earth Surf Processes* 38:1280–1298.
667 <https://doi.org/10.1002/esp.3415>
- 668 Brantley SL, White T, West N, et al Susquehanna Shale Hills Critical Zone Observatory: Shale
669 Hills in the Context of Shaver's Creek Watershed. *Vadose Zone J* 17:0.
670 <https://doi.org/10.2136/vzj2018.04.0092>
- 671 Bridgman SD, Faulkner SP, Richardson CJ (1991) Steel Rod Oxidation as a Hydrologic Indicator
672 in Wetland Soils. *Soil Science Society of America Journal* 55:856–862.
673 <https://doi.org/10.2136/sssaj1991.03615995005500030039x>

- 674 Buettner S, Kramer M, Chadwick O, Thompson A (2014) Mobilization of colloidal carbon during
675 iron reduction in basaltic soils
- 676 Caell R, Anderson M (1986) A Technique for Extensive Field Measurement of Soil Anaerobism
677 by Rusting of Steel Rods. *Forestry* 59:.. <https://doi.org/10.1093/forestry/59.2.129>
- 678 Carrière SD, Ruffault J, Pimont F, et al (2020) Impact of local soil and subsoil conditions on inter-
679 individual variations in tree responses to drought: insights from Electrical Resistivity
680 Tomography. *Sci Total Environ* 698:134247.
681 <https://doi.org/10.1016/j.scitotenv.2019.134247>
- 682 Castenson KL, Rabenhorst MC (2006) Indicator of Reduction in Soil (IRIS) Evaluation of a New
683 Approach for Assessing Reduced Conditions in Soil. *Soil Science Society of America Journal* 70:1222–1226
- 685 Chacon N, Silver W, Dubinsky E, Cusack D (2006) Iron reduction and soil phosphorus
686 solubilization in humid tropical forests soils: the roles of labile carbon pools and an electron
687 shuttle compound. *Biogeochemistry* 78:.. <https://doi.org/10.1007/s10533-005-2343-3>
- 688 Chambers RandolphM, Odum WilliamE (1990) Porewater oxidation, dissolved phosphate and the
689 iron curtain. *Biogeochemistry* 10:.. <https://doi.org/10.1007/bf00000891>
- 690 DeAngelis K, Silver W, Thompson AW, Firestone MK (2010) Microbial communities acclimate
691 to recurring changes in soil redox potential status. *Environmental Microbiology* 12:..
692 <https://doi.org/10.1111/j.1462-2920.2010.02286.x>
- 693 De-Campos A, Huang C, Johnston C (2012) Biogeochemistry of terrestrial soils as influenced by
694 short-term flooding. *Biogeochemistry*. <https://doi.org/10.1007/s10533-011-9639-2>
- 695 Dorau K, Mansfeldt T (2015) Manganese-oxide-coated redox bars as an indicator of reducing
696 conditions in soils. *Journal of environmental quality* 44:696–703
- 697 Dorau K, Mansfeldt T (2016) Manganese and iron oxide-coated redox bars as a tool to in situ study
698 the element sorption in wet soils. *Journal of Soils and Sediments* 16:976–986.
699 <https://doi.org/10.1007/s11368-015-1300-6>
- 700 Fiedler S, Vepraskas M, Richardson J (2007) Soil redox potential: importance, field
701 measurements, and observations. *Advances in Agronomy* 94:
- 702 Friedman E, Miller K, Lipson D, Angenent L (2013) Potentiostatically Poised Electrodes Mimic
703 Iron Oxide and Interact with Soil Microbial Communities to Alter the Biogeochemistry of
704 Arctic Peat Soils. *Mineral-basel* 3:318–336. <https://doi.org/10.3390/min3030318>
- 705 Friedman ES, McPhillips LE, Werner JJ, et al (2016) Methane Emission in a Specific Riparian-
706 Zone Sediment Decreased with Bioelectrochemical Manipulation and Corresponded to the
707 Microbial Community Dynamics. *Front Microbiol* 6:1523.
708 <https://doi.org/10.3389/fmicb.2015.01523>

- 709 Friedman ES, Rosenbaum MA, Lee AW, et al (2012) A cost-effective and field-ready potentiostat
710 that poised subsurface electrodes to monitor bacterial respiration. *Biosens Bioelectron*
711 32:309–313. <https://doi.org/10.1016/j.bios.2011.12.013>
- 712 Fuss CB, Driscoll CT, Johnson CE, et al (2010) Dynamics of oxidized and reduced iron in a
713 northern hardwood forest. *Biogeochemistry* 104:103–119. <https://doi.org/10.1007/s10533-010-9490-x>
- 715 Garré S, Javaux M, Vanderborght J, et al (2011) Three-Dimensional Electrical Resistivity
716 Tomography to Monitor Root Zone Water Dynamics. *Vadose Zone J* 10:412–424.
717 <https://doi.org/10.2136/vzj2010.0079>
- 718 Ginn BR, Meile C, Wilmoth J, et al (2017) Rapid iron reduction rates are stimulated by high-
719 amplitude redox fluctuations in a tropical forest soil. *Environ Sci Technology*.
720 <https://doi.org/10.1021/acs.est.6b05709>
- 721 Gosset J, Wright A (2017) Data Carpentry Python Ecology Lesson. In: Version 2017.04.0
- 722 Hall S, Silver W (2015) Reducing conditions, reactive metals, and their interactions can explain
723 spatial patterns of surface soil carbon in a humid tropical forest. *Biogeochemistry* 125:.
724 <https://doi.org/10.1007/s10533-015-0120-5>
- 725 Hall SJ, Liptzin D, Buss HL, et al (2016) Drivers and patterns of iron redox cycling from surface
726 to bedrock in a deep tropical forest soil: a new conceptual model. *Biogeochemistry*
727 130:177–190. <https://doi.org/10.1007/s10533-016-0251-3>
- 728 Hall SJ, Silver WL (2013) Iron oxidation stimulates organic matter decomposition in humid
729 tropical forest soils. *Global Change Biology* 19:2804–2813.
730 <https://doi.org/10.1111/gcb.12229>
- 731 Henderson R, Kabengi N, Mantripagada N, et al (2012) Anoxia-induced release of colloid-and
732 nanoparticle-bound phosphorus in grassland soils. *Environmental Science & Technology*
733 46:. <https://doi.org/10.1021/es302395r>
- 734 Herndon E, AlBashaireh A, Singer D, et al (2017) Influence of iron redox cycling on organo-
735 mineral associations in Arctic tundra soil. *Geochimica et Cosmochimica Acta* 207:210–
736 231. <https://doi.org/10.1016/j.gca.2017.02.034>
- 737 Herndon EM, Jin L, Brantley SL (2011) Soils Reveal Widespread Manganese Enrichment from
738 Industrial Inputs. *Environ Sci Technology* 45:241–247.
739 <https://doi.org/10.1021/es102001w>
- 740 Herndon EM, Martínez CE, Brantley SL (2014) Spectroscopic (XANES/XRF) characterization of
741 contaminant manganese cycling in a temperate watershed. *Biogeochemistry* 121:505–517.
742 <https://doi.org/10.1007/s10533-014-0018-7>

- 743 Hodges C, Brantley SL, Sharifironizi M, et al (2021) Soil carbon dioxide flux partitioning in a
744 calcareous watershed with agricultural impacts. *J Geophys Res Biogeosciences*.
745 <https://doi.org/10.1029/2021jg006379>
- 746 Hodges C, Kim H, Brantley SL, Kaye J (2019a) Soil CO₂ and O₂ Concentrations Illuminate the
747 Relative Importance of Weathering and Respiration to Seasonal Soil Gas Fluctuations. *Soil*
748 *Sci Soc Am J* 0:0. <https://doi.org/10.2136/sssaj2019.02.0049>
- 749 Hodges C, King E, Pett-Ridge J, Thompson A (2018) Potential for Iron Reduction Increases with
750 Rainfall in Montane Basaltic Soils of Hawaii. *Soil Sci Soc Am J* 82:176.
751 <https://doi.org/10.2136/sssaj2017.06.0193>
- 752 Hodges C, Mallard J, Markewitz D, et al (2019b) Seasonal and spatial variation in the potential
753 for iron reduction in soils of the Southeastern Piedmont of the US. *Catena* 180:32–40.
754 <https://doi.org/10.1016/j.catena.2019.03.026>
- 755 Huang W, Hall SJ (2017) Optimized high-throughput methods for quantifying iron
756 biogeochemical dynamics in soil. *Geoderma* 306:67–72.
757 <https://doi.org/10.1016/j.geoderma.2017.07.013>
- 758 Hunter JD (2007) Matplotlib: A 2D graphics environment. *Computing in Science & Engineering*
759 9:90–95. <https://doi.org/10.1109/MCSE.2007.55>
- 760 Jin L, Andrews DM, Holmes GH, et al (2011) Opening the “Black Box”: Water Chemistry Reveals
761 Hydrological Controls on Weathering in the Susquehanna Shale Hills Critical Zone
762 Observatory. *Vadose Zone J* 10:928. <https://doi.org/10.2136/vzj2010.0133>
- 763 Jin L, Ravella R, Ketchum B, et al (2010a) Mineral weathering and elemental transport during
764 hillslope evolution at the Susquehanna/Shale Hills Critical Zone Observatory. *Geochim*
765 *Cosmochim Ac* 74:3669–3691. <https://doi.org/10.1016/j.gca.2010.03.036>
- 766 Jin L, Ravella R, Ketchum B, et al (2010b) Mineral weathering and elemental transport during
767 hillslope evolution at the Susquehanna/Shale Hills Critical Zone Observatory. *Geochim*
768 *Cosmochim Ac* 74:3669–3691. <https://doi.org/10.1016/j.gca.2010.03.036>
- 769 Jones ME, Nico PS, Ying SC, et al (2018) Manganese-Driven Carbon Oxidation at Oxic-Anoxic
770 Interfaces. *Environ Sci Technol.* <https://doi.org/10.1021/acs.est.8b03791>
- 771 Keiluweit M, Nico PS, Kleber M, Fendorf S (2015) Are oxygen limitations under recognized
772 regulators of organic carbon turnover in upland soils? *Biogeochemistry* 127:157–171.
773 <https://doi.org/10.1007/s10533-015-0180-6>
- 774 Knorr K-H (2013) DOC-dynamics in a small headwater catchment as driven by redox fluctuations
775 and hydrological flow paths—are DOC exports mediated by iron reduction/oxidation
776 cycles? *Biogeosciences* 10:. <https://doi.org/10.5194/bg-10-891-2013>

- 777 Kraepiel AML, Dere AL, Herndon EM, Brantley SL (2015a) Natural and anthropogenic processes
778 contributing to metal enrichment in surface soils of central Pennsylvania. *Biogeochemistry*
779 265–283. <https://doi.org/10.1007/s10533-015-0068-5>
- 780 Kraepiel AML, Dere AL, Herndon EM, Brantley SL (2015b) Natural and anthropogenic processes
781 contributing to metal enrichment in surface soils of central Pennsylvania. *Biogeochemistry*
782 265–283. <https://doi.org/10.1007/s10533-015-0068-5>
- 783 van der Lee, G. E., de Winder, B., Bouten, W., & Tietema, A. (1999). Anoxic microsites in
784 Douglas fir litter. *Soil Biology and Biochemistry*, 31(9), 1295-1301.
- 785 Lin H, Kogelmann W, Walker C, Bruns M (2006) Soil moisture patterns in a forested catchment:
786 A hydropedological perspective. *Geoderma* 131:345–368
- 787 Linkhorst A, Dittmar T, Waska H (2016) Molecular fractionation of dissolved organic matter in a
788 shallow subterranean estuary: the role of the iron curtain. *Environmental Science &*
789 *Technology*. <https://doi.org/10.1021/acs.est.6b03608>
- 790 Lipson D, Jha M, Raab T, Oechel WC (2010) Reduction of iron (III) and humic substances plays
791 a major role in anaerobic respiration in an Arctic peat soil. *Journal of Geophysical Research*
792 115:. <https://doi.org/10.1029/2009JG001147>
- 793 Logan BE, Rossi R, Ragab A, Saikaly PE (2019) Electroactive microorganisms in
794 bioelectrochemical systems. *Nat Rev Microbiol* 17:307–319.
795 <https://doi.org/10.1038/s41579-019-0173-x>
- 796 Lovley DR, Phillips EJ (1988) Novel mode of microbial energy metabolism: organic carbon
797 oxidation coupled to dissimilatory reduction of iron or manganese. *Applied and*
798 *environmental microbiology* 54:1472–1480
- 799 Ma D, Wu J, Yang P, Zhu M (2020) Coupled Manganese Redox Cycling and Organic Carbon
800 Degradation on Mineral Surfaces. *Environ Sci Technol* 54:8801–8810.
801 <https://doi.org/10.1021/acs.est.0c02065>
- 802 McKinney W (2010) Data Structures for Statistical Computing in Python. In: Walt S van der,
803 Millman J (eds) *Proceedings of the 9th Python in Science Conference*. pp 56–61
- 804 Michot D, Benderitter Y, Dorigny A, et al (2003) Spatial and temporal monitoring of soil water
805 content with an irrigated corn crop cover using surface electrical resistivity tomography:
806 SOIL WATER STUDY USING ELECTRICAL RESISTIVITY. *Water Resour Res* 39:.
807 <https://doi.org/10.1029/2002wr001581>
- 808 Owens P, Wilding L, Miller W, Griffin R (2008) Using iron metal rods to infer oxygen status in
809 seasonally saturated soils. *Catena* 73:197–203
- 810 Parkin, T.B. (1987), Soil Microsites as a Source of Denitrification Variability. *Soil Science Society
811 of America Journal*, 51: 1194-1199.
812 <https://doi.org/10.2136/sssaj1987.03615995005100050019x>

- 813 Patrick WH, Jugsujinda A (1992) Sequential Reduction and Oxidation of Inorganic Nitrogen,
814 Manganese, and Iron in Flooded Soil. *Soil Sci Soc Am J* 56:1071–1073.
815 <https://doi.org/10.2136/sssaj1992.03615995005600040011x>
- 816 Peters V, Conrad R (1996) Sequential reduction processes and initiation of CH₄ production upon
817 flooding of oxic upland soils. *Soil Biology and Biochemistry* 28:371–382
- 818 Pett-Ridge J, Silver WL, Firestone MK (2006) Redox Fluctuations Frame Microbial Community
819 Impacts on N-cycling Rates in a Humid Tropical Forest Soil. *Biogeochemistry* 81:95–110.
820 <https://doi.org/10.1007/s10533-006-9032-8>
- 821 Rabenhorst M, Hively W, James B (2009) Measurements of soil redox potential. *Soil Science
822 Society of America Journal* 73:668–674
- 823 Rabenhorst MC, Burch S (2006) Synthetic iron oxides as an indicator of reduction in soils (IRIS).
824 *Soil Science Society of America Journal* 70:1227–1236
- 825 Renault P, Stengel P (1994) Modeling oxygen diffusion in aggregated soils: I. Anaerobiosis inside
826 the aggregates
- 827 Samouëlian A, Cousin I, Tabbagh A, Bruand A (2005) Electrical resistivity survey in soil science:
828 a review. *Soil and Tillage Research* 83:
- 829 Schaetzl RJ, Rothstein DE (2016) Temporal variation in the strength of podzolization as indicated
830 by lysimeter data. *Geoderma* 282:26–36. <https://doi.org/10.1016/j.geoderma.2016.07.005>
- 831 Scott B, Baldwin AH, Yarwood S, et al (2021) Macro and microscopic visual imaging tools to
832 investigate metal reducing bacteria in soils. *Soil Sci Soc Am J* 85:184–192.
833 <https://doi.org/10.1002/saj2.20171>
- 834 Sexstone A, Parkin T (1985) Temporal response of soil denitrification rates to rainfall and
835 irrigation. *Soil Science Society of America Journal* 49:
- 836 Stiles CA, Dunkinson ET, Ping C, Kidd J (2010) Initial field installation of manganese indicators
837 of reduction in soils, Brooks Range, Alaska. *Soil Survey Horizons* 51:102–107
- 838 Stumm W, Morgan JJ (1996) Aquatic Chemistry
- 839 team T pandas development (2020) pandas-dev/pandas: Pandas. Version latest. Zenodo. URL
840 <https://doi.org/10.5281/zenodo.3509134>
- 841 Thompson A, Chadwick OA, Rancourt DG, Chorover J (2006) Iron-oxide crystallinity increases
842 during soil redox oscillations. *Geochimica et Cosmochimica Acta* 70:1710–1727
- 843 Verchot LV, Davidson EA, Cattâniao JH, Ackerman IL (2000) Land-Use Change and
844 Biogeochemical Controls of Methane Fluxes in Soils of Eastern Amazonia. *Ecosystems*
845 3:41–56. <https://doi.org/10.1007/s100210000009>

- 846 Viollier E, Inglett PW, Hunter K, et al (2000) The ferrozine method revisited: Fe(II)/Fe(III)
847 determination in natural waters. Appl Geochem 15:785–790.
848 [https://doi.org/10.1016/s0883-2927\(99\)00097-9](https://doi.org/10.1016/s0883-2927(99)00097-9)
- 849 Virtanen P, Gommers R, Oliphant TE, et al (2020) SciPy 1.0: Fundamental Algorithms for
850 Scientific Computing in Python. Nature Methods 17:261–272.
851 <https://doi.org/10.1038/s41592-019-0686-2>
- 852 Waskom ML (2021) seaborn: statistical data visualization. Journal of Open Source Software
853 6:3021. <https://doi.org/10.21105/joss.03021>
- 854 Yesavage T, Fantle MS, Vervoort J, et al (2012) Fe cycling in the Shale Hills Critical Zone
855 Observatory, Pennsylvania: An analysis of biogeochemical weathering and Fe isotope
856 fractionation. Geochimica et Cosmochimica Acta 99:18–38
- 857 Zausig, J., Stepniewski, W. and Horn, R. (1993), Oxygen Concentration and Redox Potential
858 Gradients in Unsaturated Model Soil Aggregates. Soil Science Society of America Journal,
859 57: 908-916. <https://doi.org/10.2136/sssaj1993.03615995005700040005x>